Catalysis Science & Technology

ROYAL SOCIETY OF CHEMISTRY

PAPER

View Article Online
View Journal | View Issue

Cite this: *Catal. Sci. Technol.*, 2023, **13**, 5989

Three-dimensional ordered macroporous cerium–manganese composite oxide for NO oxidation†

Canyang Qu,[a] Ping Wang,[a] Miao He,[a] Cheng Yang,[a] Jing Xiong,[b] Xiaohua Sun,*[a] Yuechang Wei *[b] and Zhenxing Li *[a]

Received 29th July 2023,
Accepted 7th September 2023

DOI: 10.1039/d3cy01059g

rsc.li/catalysis

NO_x is one of the main sources of air pollution, which primarily comes from automobile exhausts. Rare earth-based catalysts for NO oxidation have excellent oxygen storage and release performance and good structural stability. Herein, a series of three-dimensional ordered microporous (3DOM) cerium–manganese composite oxide catalysts with different cerium–manganese ratios for NO oxidation were prepared by the sol–gel method. The 3DOM structure improves the contact efficiency of the NO, soot and the catalyst. By incorporating Mn^{3+} ions into the cerium oxide lattice, a Ce–Mn solid solution forms with an ordered macroporous structure, and the interaction between cerium and manganese significantly increases the amount of reactive oxygen species. The catalyst with the optimal cerium–manganese ratio (1 : 2) was able to achieve a conversion rate of 62% at 250 °C, and the highest conversion rate reached 98%, which is far higher than pure cerium oxide and pure manganese oxide catalysts. This work provides a promising catalyst for NO oxidation and soot combustion applications.

1. Introduction

The increasing number of automobiles has exacerbated the serious problem of environmental pollution,[1,2] especially with regards to air pollution.[3] NO_x is one of the main sources of air pollution, which primarily comes from automobile exhausts. Not only is NO_x highly toxic, potentially causing lesions and even cancer in humans,[4,5] but it also participates in the formation of haze and photochemical smog with sulfur dioxide[6,7] and inhalable particulate matter, posing a huge threat to the environment and human health.[8,9] In addition, NO_2 produced by NO_x oxidation has better oxidation properties than O_2, which is more conducive to soot combustion.[10] The catalytic combustion technology, with the advantages of low energy consumption,[11,12] high catalytic efficiency and almost no secondary pollution,[13,14] has been widely used in the industrial treatment of NO_x. The most critical thing for catalytic combustion is a reaction system with multiple reactions. Currently, the most commonly used metal catalysts are divided into two categories: precious metal catalysts[15,16] and non-precious metal catalysts.[17,18] The active components of precious metal catalysts are Pt, Pd, Au (ref. 19 and 20) and other precious metals. Although they have high catalytic activity and good sulfur resistance,[21] they are prone to catalyst poisoning,[22,23] and the active components are prone to volatilization and sintering, making them expensive and difficult to preserve. Therefore, non-precious metal catalysts with the advantages of good toxicity resistance, low cost and high thermal stability have garnered significant attention. The main active centers include Cu,[24,25] Mn,[26,27] Co, Ce (ref. 28) and other metallic elements.[29,30] The rare earth-based catalyst CeO_2 has excellent oxygen storage and release performance, good structural stability and relatively high specific surface area,[31] but pure cerium dioxide has low activity and thermal stability,[32] and its structure can easily be affected at high temperature, which limits its practical applications. Therefore, strategies such as adding or loading other metals and preparing different morphologies are often used to improve the catalytic performance.[33] Meanwhile, the pore size of the traditional catalyst is less than 10 nm, which is not conducive to the flow of pollutants in the catalyst. The three-dimensional ordered macropore (3DOM) refers to the orderly arrangement of pore structures in three-dimensional space, and the pore size is larger than 50 nm, which can enable diesel vehicle particles with large particle sizes to enter pore channels and fully react with the catalysts.[34,35]

In this paper, building upon the excellent oxygen storage performance of cerium dioxide, manganese was introduced and combined with the advantages of a 3DOM structure. Cerium and manganese composite oxides with various ordered macroporous structures with different cerium–

[a] State Key Laboratory of Heavy Oil Processing, College of New Energy and Materials, China University of Petroleum (Beijing), Beijing 102249, China. E-mail: hua82@126.com, lizx@cup.edu.cn
[b] College of Science, China University of Petroleum (Beijing), Beijing 102249, China. E-mail: weiyc@cup.edu.cn

† Electronic supplementary information (ESI) available. See DOI: https://doi.org/10.1039/d3cy01059g

manganese molar ratios were prepared *via* the excessive impregnation method using polymethyl methacrylate (PMMA) as a hard template. These cerium–manganese composite oxide catalysts exhibit regular ordered macroporous structures, and the average pore size is about 300 nm. The catalyst with the best cerium–manganese ratio was able to achieve a conversion rate of 62% at 250 °C, and the highest conversion rate reached 98%, which is far higher than pure cerium oxide and pure manganese oxide catalysts. Additionally, the carbon soot performance was also improved. With the increase of Mn doping, the macroporous structure is improved. When the cerium–manganese ratio is 1 : 2, the cerium–manganese composite oxide catalyst shows a high-quality three-dimensional ordered macroporous structure with the largest specific surface area and a thin and complete pore wall, which is conducive to diffusion and transfer between substances. On the other hand, due to the formation of the cerium–manganese solid solution, the synergistic effect between cerium and manganese means the reaction can be carried out at low temperatures. This low-cost, environmentally friendly, highly stable and highly active catalyst is expected to improve the catalytic performance through the macroporous effect and the synergistic effect between cerium and manganese. Based on the experimental results, the possible mechanism of catalyst oxidation of NO_x and soot combustion is discussed.

2. Experimental

2.1. Material preparation

2.1.1 Preparation of PMMA microspheres. A three-neck round-bottom flask (1000 ml) was used as the reaction device. 440 ml of deionized water was added before the reaction, which was sealed with plastic wrap and connected to a condensing device. During the reaction, nitrogen was continuously injected and stirred at a constant rate of 350 r min^{-1}. After stirring for 20 min, a 50 ml solution containing 0.6 g potassium persulfate was added and heated to 80 °C. The reaction was continued for 2 h and then stopped. The obtained PMMA emulsion was set aside and then filtered using a microporous filter membrane. A part of the filtered emulsion was centrifuged for 10 h at a centrifugation rate of 3000 r min^{-1} to obtain PMMA microspheres arranged in an orderly manner. After the supernatant was poured away, the obtained PMMA microspheres were dried at room temperature, and finally the green-colored PMMA templates were obtained in an orderly arrangement.

2.1.2 Preparation of the ordered macroporous manganese–cerium oxide catalyst. The ordered macroporous catalyst was prepared by a template method. A certain amount of $C_4H_{14}MnO_8$ and Ce $(NO_3)_3{\cdot}6H_2O$ were put into a 50 ml beaker. At the same time, CH_3OH and $(CH_2OH)_2$ with a ratio of 1 : 4 were added into 40 ml, heated to 50 °C and stirred to dissolve the metal salt completely. Four kinds of precursor solutions with different proportions were obtained by adjusting the weight of metal salts added, and a group of pure cerium oxide solution and pure manganese oxide solution were used to compare the properties, namely CM1 (cerium–manganese ratio 1 : 1), CM2 (cerium–manganese ratio 1 : 2), CM3 (cerium–manganese ratio 1 : 3), CM4 (cerium–manganese ratio 1 : 4), CeO_2 and Mn_2O_3.

First, the PMMA microspheres were placed into the prepared metal salt solution and put into a vacuum drying oven. After 24 h of vacuum impregnation at room temperature, the Brinell funnel was used for filtration. The mixed solid obtained after filtration was placed into a drying oven at 60 °C for 24 h. Finally, the temperature gradient method was used for calcination. The dried solid mixture and alumina pellets were layered in the dry quartz tube. The PMMA template is removed by the tube furnace under air atmosphere at a heating rate of 1 °C min^{-1} after 270 min heating from 30 °C to 300 °C for 3 h calcination. Under the atmosphere of air, after 250 minutes of calcination from 300 °C to 550 °C at a heating rate of 1 °C min^{-1}, the three-dimensional ordered macropore cerium–manganese catalyst was obtained after the tubular furnace was reduced to room temperature.

2.2. Material characterization and catalytic performance

The catalyst activity was tested in a fixed-bed reactor with a diameter of 30 mm and a length of 500 mm. The 0.025 g sample was weighed and placed into a quartz tube. 40 mg cm^{-3} nitrogen was injected into the gas pool of infrared chromatography in front of the reaction to eliminate other gases inside. After clearing the background, 5 mg cm^{-3} nitric oxide as a pollutant and 2.8 mg cm^{-3} oxygen were injected.

NO conversion is defined as follows:

$$\text{NO conversion} = ([\text{NO}]_{in} - [\text{NO}]_{out})/[\text{NO}]_{in} \times 100\%$$

Soot-TPO was tested in a fixed bed reactor with a diameter of 30 mm and a length of 500 mm. The 0.025 g sample was weighed and placed in a quartz tube. During the reaction, 25 mg cm^{-3} nitrogen, 19 mg cm^{-3} nitric oxide and 2.5 mg cm^{-3} oxygen were injected into the fixed bed reactor. First, it was heated from 30 °C to 150 °C for 12 minutes, and then 200 min to 550 °C at 2 °C min^{-1}. The mixing was performed by mixing the catalyst and soot in loose contact.

During the hydrogen programmed temperature reduction (H_2-TPR) test, 50 mg catalysts (40–60 mesh) were pretreated in a U-shaped fluidized bed quartz microreactor at 200 °C in a 50 mL min^{-1} argon stream for 1 hour and then cooled to 100 °C. After the pretreatment, the catalyst was reduced at a flow rate of 10 vol%H_2/Ar (30 mL min^{-1}) at a heating rate of 10 °C min^{-1} in a temperature range of 100–900 °C. H_2 consumption was recorded by using a thermal conductivity detector (TCD). The surface area of the catalyst was determined using a BSD-660M A3M analyzer based on N_2 adsorption–desorption at 80 °C and the degassing time was 4 hours.

In situ diffuse infrared Fourier transform (DRIFT) spectroscopy was tested on the IRTracer-100 infrared

spectrometer at Shimadzu Manufacturing in Japan. First, the impurities were removed at a flow rate of 46.1 ml min^{-1} under nitrogen, and then the background spectra were collected at the same flow rate from 450 °C with a decrease of 50 °C each time.

2.3. Materials

Manganese acetate tetrahydrate ($C_4H_{14}MnO_8$), Shanghai Aladdin Biochemical Technology Co., LTD.; potassium persulfate ($K_2S_2O_8$), Shanghai Aladdin Biochemical Technology Co., LTD.; cerous nitrate hexahydrate Ce $(NO_3)_3{\cdot}6H_2O$, Shanghai Aladdin Biochemical Technology Co., LTD.; methyl methacrylate (mma), Shanghai Mlin Biochemical Technology Co., LTD.; methanol (CH_3OH), Tianjin Jindong Tianzheng Fine Chemical Reagent Factory; and ethylene glycol $(CH_2OH)_2$, Tianjin Jindong Tianzheng Fine Chemical Reagent Factory were obtained.

3. Results and discussion

The synthesis strategy of the cerium–manganese composite oxide with a three-dimensional ordered microporous (3DOM) structure is shown in Scheme 1. First, the polymethyl methacrylate (PMMA) microspheres were prepared as the hard template, and then cerium and manganese salts were impregnated into the gaps of the microspheres by the sol–gel method. Finally, the microsphere template was burned off to obtain the cerium–manganese composite oxide with a three-dimensional ordered microporous (3DOM) structure. Fig. 1 shows the SEM images of the six as-prepared catalysts. The pore wall of pure cerium oxide is angular and stable (Fig. 1a), connected by an aperture window of approximately 50 nm. The pore walls are closely distributed, and pore wall fracture rarely occurs, which is attributed to the stable structure and large wall thickness of cerium oxide. The pore size of pure manganese oxide is uneven, about 250 nm–350 nm (Fig. 1b) and pore wall fracture occurs, and some macropores undergo structural collapse, which can lead to the deterioration of permeability and the reduction of the specific surface area.[36] The wall thickness of the manganese oxide macroporous structure is lower than that of cerium oxide, and the pore wall is collapsed, which cannot maintain the stability of the pore structure. In Fig. 1c–f, the 3DOM cerium–manganese composite oxide has a uniform, ordered and tightly arranged macroporous structure. The macropore size is about 280 nm, which is smaller than that of the methyl methacrylate microsphere (340–370 nm) as the precursor template. This smaller porous size than the template is attributed to the slight shrinkage of the overall structure during the calcination of the precursor template and the sintering of the cerium–manganese oxide.[37] The highly ordered macropores are periodically connected with each other through a window of about 100 nm, and almost no agglomeration particles are observed on the surface, indicating that Mn^{3+} is highly dispersed on the surface of the macroporous structure. This kind of large pore structure is suitable for a gas–solid reaction, and the large pore size of about 280 nm is prone to allow pollutants to enter the inner pore and come into full contact with the catalyst.[38] Therefore, this structure can effectively reduce the mass transfer resistance. In addition, it can be observed from the energy-dispersive X-ray spectroscopy (EDS) elemental mapping that cerium and manganese elements are evenly distributed on the catalyst with the increase of manganese content, the EDS image of manganese element becomes clearer, while the color of the cerium element distribution image becomes lighter. The results of the EDS images are consistent with the feed ratio of cerium–manganese (Fig. 1g and S1†).

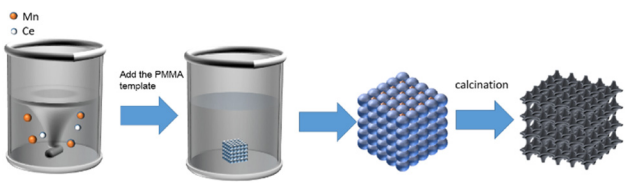

Scheme 1 Synthesis strategy of the cerium–manganese composite oxide with a 3DOM structure.

Fig. 2a shows the wide-angle X-ray diffraction pattern (XRD) of 3DOM structures CM1 (cerium–manganese ratio 1 : 1), CM2 (cerium–manganese ratio 1 : 2), CM3 (cerium–manganese ratio 1 : 3), CM4 (cerium–manganese ratio 1 : 4), CeO_2 and Mn_2O_3 catalysts. The characteristic peaks of CeO_2, CM1, CM2, CM3 and CM4 at 28.8°, 33.4°, 47.6°, 56.5°, respectively, correspond to the crystal faces (111), (200), (220) and (311) of cerium oxide with a face-centered cubic fluorite structure (PDF: 43-1002),[39] indicating that the five catalysts of CeO_2, CM1, CM2, CM3 and CM4 formed a face-centered cubic fluorite structure of cerium oxide after calcination. The characteristic diffraction peaks of Mn_2O_3 mainly appear at 23.3°, 33.2°, 38.5°, 45.1°, 49.6°, 55.5° and 66.8°, which correspond to the crystal planes of (211), (222), (400), (332), (431), (440) and (622) (PDF: 41-1442).[40] When the cerium–manganese ratio is 1 : 1, the diffraction peak of manganese oxide can hardly be observed, but only the diffraction peak of cerium oxide can be observed, indicating that manganese oxide is uniformly dispersed in the cerium oxide lattice to form the cerium–manganese solid solution.[41] With increasing manganese content, the characteristic peaks of manganese oxide gradually appear. Therefore, the CM2, CM3 and CM4 is cerium–manganese composite oxide. Raman spectroscopy is a practical characterization method that can be used to study the mobility of atoms in a lattice. Fig. 2b shows the Raman spectrum of CeO_2, and a clear peak at 462 cm^{-1} can be attributed to the triple degenerate F_{2g} mode and the stretching of the Ce–O symmetric vibration unit is attributable to the fluorite structure of CeO_2.[42] For Mn_2O_3, two distinct Raman peaks at 656 cm^{-1} and 310 cm^{-1} can be observed in Fig. 2b, which correspond to the Mn–O stretching pattern of Mn_2O_3 (ref. 43) and the asymmetric bridging oxygen species of Mn–O–Mn, respectively.[44] For the CM1 catalyst, the Raman peak shifts to the left to 452 cm^{-1}.

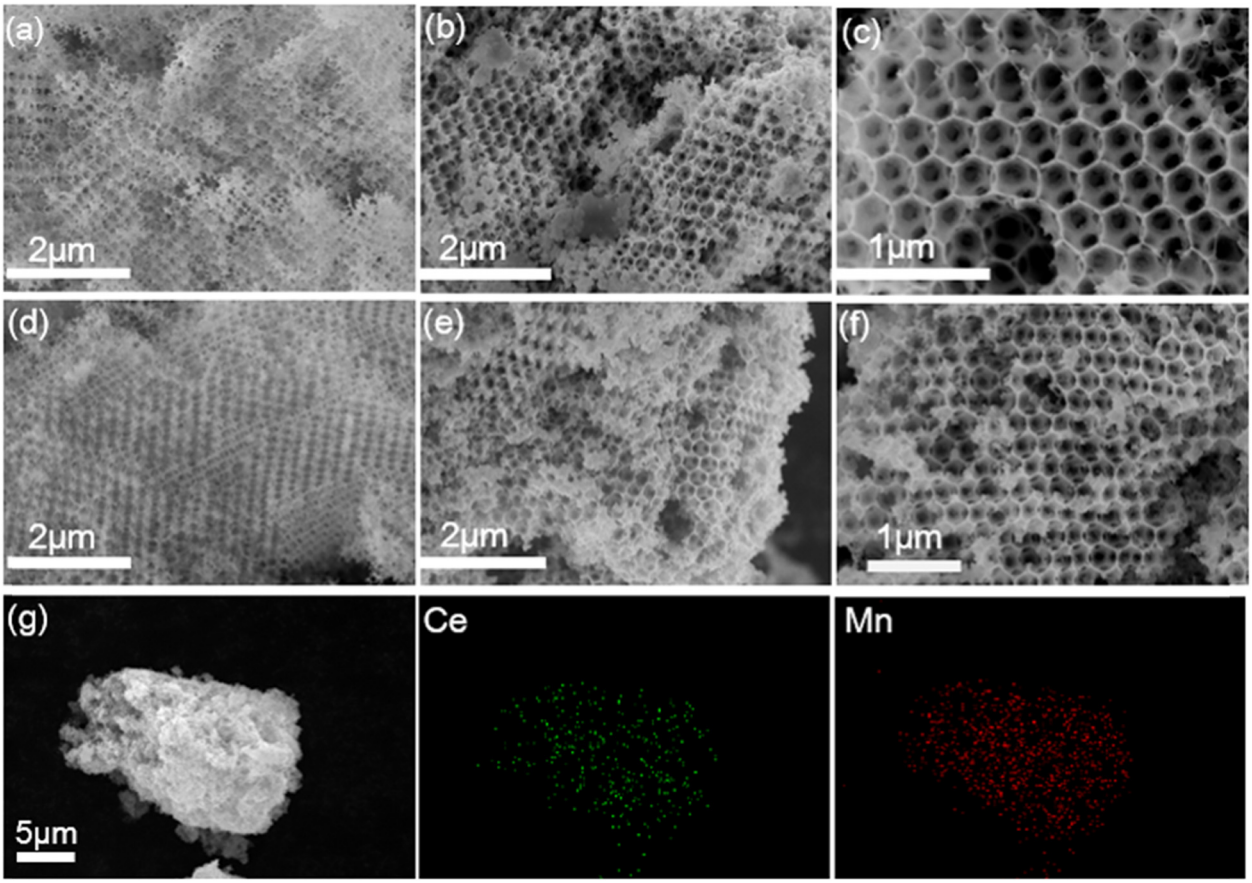

Fig. 1 Three dimensional ordered manganese–cerium oxides with different cerium–manganese ratios: (a) CeO_2, (b) Mn_2O_3, (c) CM1, (d) CM2, (e) CM3, (f) CM4 and EDS of CM2 (g).

However, the Mn^{3+} cation is smaller than the Ce^{4+} cation, so it is expected that the shift in the F_{2g} band will occur towards higher Raman shift values; however, the opposite trend is observed. This unexpected shift could be due to the partial reduction of cerium(IV) to cerium(III) to compensate for the lattice shrinkage caused by the insertion of Mn^{3+} into the cerium oxide lattice.[45] The formation of oxygen vacancies at the same time is due to the insertion of Mn^{3+} and partial reduction of Ce^{4+} to Ce^{3+}. Subsequently, with the increase in manganese content, the Raman peak of cerium oxide with a fluorite structure from CM2 began to shift from 470 cm^{-1} to the right, which conforms to the trend of Mn^{3+} insertion into the cerium oxide lattice.[43] At the same time, a Raman peak with the obvious characteristics of manganese oxide appears from CM2 (located at 628 cm^{-1}). As Ce^{4+} is incorporated into the lattice of manganese oxide and the ionic radius of Ce^{4+} is larger than Mn^{3+}, the Raman peak is shifted to the left. Similarly, it is later observed that the Raman peak of CM3 belonging to Mn_2O_3 is located at 652 cm^{-1}, which is also due to this reason. With the further reduction of cerium content, the Raman peak position of CM4 returns to 656 cm^{-1}. The nitrogen adsorption and desorption isotherms of cerium–manganese composite oxides with different cerium–manganese ratios are shown in Fig. 2c. The six catalysts all exhibit type II adsorption and desorption isotherms, and H3 hysteresis loops are formed when the relative pressure (P/P_0) is 0.8–1.0,[46] which reveals that the six catalysts all form large pore structures, but the shape of the hysteresis loops is different, indicating that the pore structures of each catalyst are different, which is consistent with the SEM analysis results. It can be seen from the BET results that CeO_2 has a larger specific surface area than Mn_2O_3 due to its structural stability. Therefore, the specific surface area of cerium–manganese composite oxide is better than Mn_2O_3. Among them, the CM2 catalyst has the largest specific surface area (60 $m^2\ g^{-1}$) among the composite oxide catalysts (Table S1†).

In order to study the electronic structure of surface elements, X-ray photoelectron spectroscopy (XPS) was used to analyze the ion content and oxidation state of six kinds of 3DOM catalysts. The 3d spectrum of Ce is shown in Fig. 2d and eight peaks can be fitted from the XPS spectrum of Ce 3d. The six peaks labeled (a1, a2, a3) and (b1, b2, b3) correspond to Ce^{4+} 3d 3/2 and Ce^{4+} 3d 5/2, respectively. The other two peaks a and b correspond to Ce^{3+} 3d 3/2 and Ce^{3+} 3d 5/2, respectively.[43] The peak strength of Ce^{4+} in all the catalysts is much greater than that of Ce^{3+}, indicating that cerium(IV) is the main valence state.[47] The presence of Ce^{3+} can provide more oxygen vacancies to the catalyst and

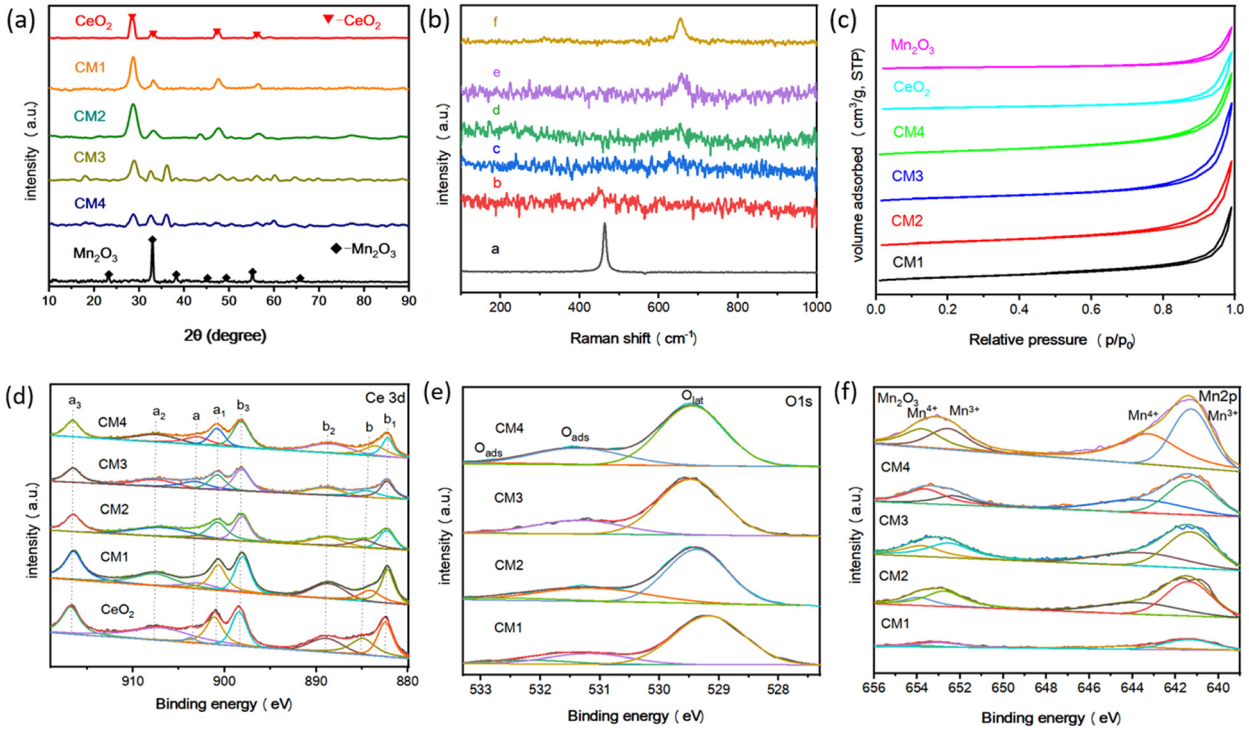

Fig. 2 (a) XRD of cerium–manganese oxide catalysts with different proportions of 3DOM. (b) Raman spectra of 3DOM samples. a. CeO_2, b. CM1, c. CM2, d. CM3, e. CM4, f. Mn_2O_3. (c) Adsorption and desorption isotherm of cerium–manganese complex oxides with different cerium–manganese ratios of 3DOM. XPS spectra of (d) Ce 3d, (e) Mn 2p, and (f) O1s.

accelerate the electron transfer, and Table S2† shows that the specific contents of Ce^{3+} are different. CeO_2 and CM1 have the lowest Ce^{3+} content, while the introduction of manganese element significantly increases the Ce^{3+} content (Table S2†). Fig. 2e shows the XPS of Mn 2p and the XPS double peaks of Mn 2p can be observed. Binding energies at approximately 641.5 eV and 653.4 eV are attributed to Mn 2p 3/4 and Mn 2p 1/2, respectively.[48] In all the samples, Mn is present in a mixture of Mn^{3+} and Mn^{4+} valence states. The relative content of manganese ions is calculated according to the corresponding peak area of the spectrum, and the obtained values are listed in Table S2.† The increase of the content of valence state species leads to the imbalance of the surface charge of the catalyst, increases the electron transfer rate, and promotes the formation of a large number of oxygen vacancies and unsaturated structures.[47] It can be seen from Table S2† that CM2 has the highest content of Mn^{3+}. The O1s spectra of different catalysts are shown in Fig. 2f and the two peaks at 531.8 eV and 529.7 eV are attributed to lattice oxygen atoms (O_{latt}) and surface adsorbed oxygen (O_{ads}), respectively.[48] Compared with lattice oxygen, the surface adsorbed oxygen is more mobile and has higher activity in low temperature oxidation. The lattice oxygen basically reacts in the high temperature region. CM2 has the highest number of adsorbed oxygen sites, which play an important role in the oxidation reaction.[47] Based on the above experimental results, the CM2 has the highest Mn^{3+} and surface reactive oxygen species, and also has a high Ce^{3+} content, suggesting that CM2 is an excellent catalyst for NO oxidation.

The NO oxidation of the catalysts was evaluated under a gradient temperature increase of 5 vol%O_2 and 500 ppm NO (Fig. 3a and b). For pure cerium oxide, the program is heated until 250 °C, and there is still no catalytical activity. The highest conversion rate (34.4%) is at nearly 400 °C. The pure cerium oxide with low activity is obviously not in line with the conditions of practical application. The performance of pure manganese oxide is slightly better than that of cerium oxide in the programmed gradient temperature increase. The manganese oxide starts to show activity after 250 °C, and the conversion rate is close to that of cerium–manganese composite oxide catalysts, and the catalytic activity is even slightly better than that of the cerium–manganese composite catalyst (CM1) in the high temperature region. The maximum conversion rate reaches 49.9% at 350 °C, which is higher than the maximum conversion rate of 20.8% at 316 °C for CM1. However, the activity of cerium–manganese composite oxides (CM2, CM3 and CM4) far exceeds that of pure cerium dioxide and pure manganese dioxide at all temperatures, which indicates that the different cerium–manganese ratio has a certain effect on the catalyst activity. The catalyst with the best overall performance is CM2, which maintains a high conversion rate in the low and high temperature regions, and reaches the highest conversion rate of 97.9% at 325 °C. For the consideration of practical application, we only compare the performance of the activity in the lower temperature zone

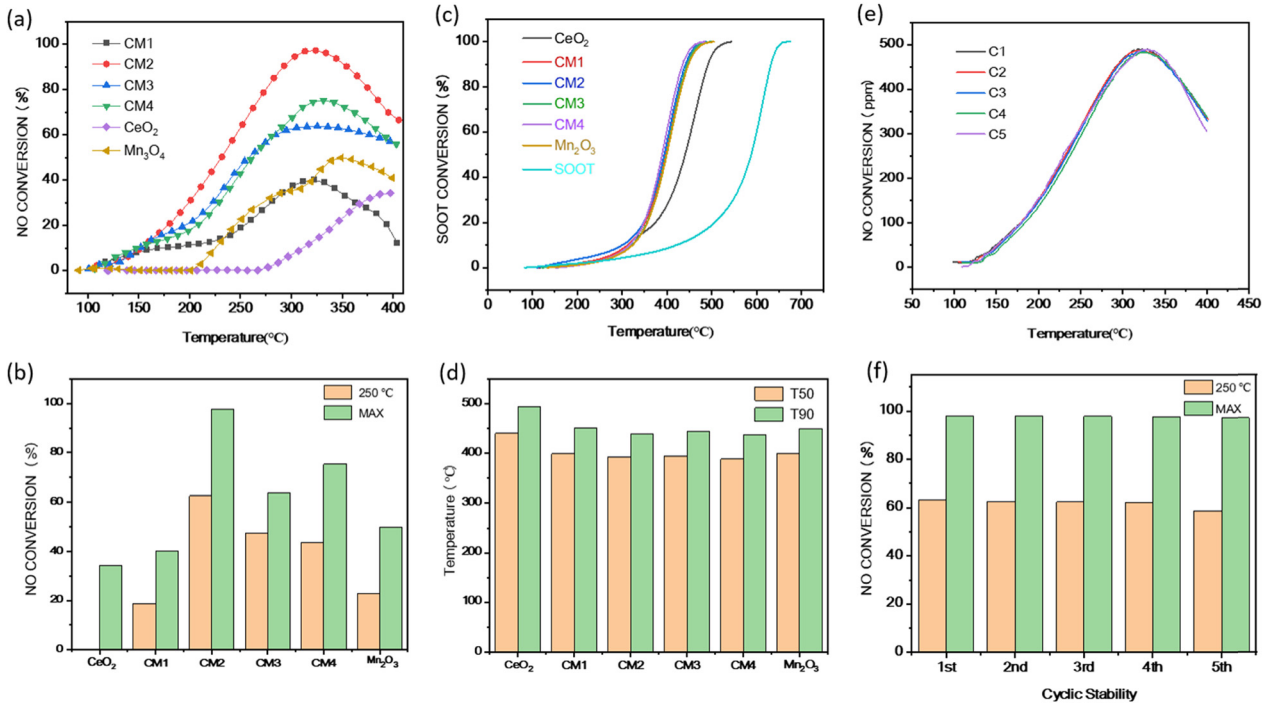

Fig. 3 (a) NO_2 concentration of the catalysts under N_2 air flow during a gradient temperature increase of 5 vol%O_2 and 500 ppm NO. (b) Different cerium–manganese ratios of 3DOM cerium–manganese composite oxide NO-TPO conversion rate and conversion rate of 250 °C. (c) Soot combustion curves of cerium–manganese composite oxides with different cerium–manganese ratios of 3DOM and temperature distribution of T50 and T90 (d). (e) The cyclic test was performed at 5 vol%O_2, 500 ppm NO and N_2 as the equilibrium gas. (f) Conversion rate and maximum conversion rate at 250 °C.

at 250 °C, and the NO conversion activity order at 250 °C is CM2 > CM3 > CM4 > CM1 > Mn_2O_3 > CeO_2. For different catalysts CM1, CM2, CM3 and CM4, the highest conversion temperature is 322 °C, 325 °C, 325 °C and 331 °C, respectively, and the highest conversion temperature is lower than that of pure cerium and pure manganese catalysts. Therefore, the cerium–manganese composite oxide shows a better performance than the single metal oxide.[49]

The soot combustion reaction is a heterogeneous reaction with solid soot as the reactant. The presence of NO can also promote soot oxidation, as NO_2 has excellent oxidation properties compared to O_2. Therefore, the ability of NO to oxidize to NO_2 on the catalyst plays a key role in soot combustion. The mass ratio of catalyst to soot was 10 : 1. The carbon fume oxidation performance of CM1, CM2, CM3, CM4, CeO_2 and Mn_2O_3 catalysts and a control group of pure soot was also studied under N_2 flow during the gradient temperature rise of 5 vol%O_2 and 500 ppm NO as oxidants. Fig. 3c and d show the soot combustion curves of different catalysts, and the performance of all the catalysts is better than that of pure soot combustion. Compared with pure cerium dioxide, the catalytical activity of Mn_2O_3 and CM1–CM4 is significantly better than the former. Table 1 shows the specific soot combustion temperatures of each catalyst at T10, T50 and T90 (soot conversion rate of ten percent (T10), fifty percent (T50) and ninety percent temperature (T90)).[50] For cerium oxide, the temperatures of T10, T50 and T90 are 315 °C, 441 °C and 494 °C, respectively, while the temperatures of manganese oxide are 325 °C, 400 °C and 450 °C, respectively. The performance of manganese oxide is better than that of cerium oxide. The temperatures of T10, T50 and T90 of CM2 with the best performance are 307 °C, 393 °C and 440 °C, respectively, which is consistent with NO conversion. Based on the above experiential results, CM1 is an excellent NO oxidation and soot combustion catalyst.

To evaluate the stability, the CM2 sample was selected to test the stability in the NO oxidation reaction. Over the five test cycles, the catalyst heated up at the same heating rate and passed through the same air flow to ensure that the NO oxidation operated under the same conditions each time in Fig. 3e and f. As shown in Fig. 3e, at 250 °C, the conversion rate decreased within 1% from the first cycle to the fifth cycle and decreased 58.8% from 62.6% to the fifth cycle. The maximum conversion rate remained between 97–98% and the temperature at the maximum conversion rate was similar. Therefore, the catalyst has good stability in the NO oxidation

Table 1 Specific combustion temperatures of different catalysts

Catalysts	T10	T50	T90
CeO_2	315 °C	441 °C	494 °C
Mn_2O_3	325 °C	400 °C	450 °C
CM1	320 °C	399 °C	452 °C
CM2	307 °C	393 °C	440 °C
CM3	317 °C	395 °C	445 °C
CM4	314 °C	389 °C	438 °C
Soot	426 °C	588 °C	635 °C

reaction. In addition, Fig. S2† shows the test results of soot combustion cycle stability. After each test, the temperature increases of T50 and T90 are within 10 °C, which shows a good soot combustion stability.

Fig. 4a shows the H_2-TPR curves of different cerium–manganese ratios. The region below 400 °C belongs to the low temperature region, 400–600 °C belongs to the medium temperature region, and above 600 °C belongs to the high temperature region, that is, the temperature range at which oxygen species basically do not participate in the reaction. The reduction peaks of pure cerium dioxide catalyst appear at about 394 °C, 499 °C and 711 °C. The reduction peak at 394 °C corresponds to the reduction of adsorbed oxygen on the surface of cerium oxide, 499 °C corresponds to the reduction of Ce^{4+} in the outermost layer, and 711 °C corresponds to the reduction peak of lattice oxygen in CeO_2.[43] Two reduction peaks are observed for pure manganese oxide catalysts. The lower reduction peak at 334 °C corresponds to the reduction of Mn_2O_3 to Mn_3O_4, while the second peak at 496 °C is attributed to the subsequent reduction of Mn_3O_4 to MnO.[51] CM1 and CM2 both have three reduction peaks belonging to CeO_2. Compared with pure cerium oxide, the reduction peaks in the low temperature region move significantly to lower temperatures. Peaking at a lower temperature indicates that the catalyst has better activity at low temperatures and is more in line with the requirements of practical applications. At the same time, all catalysts showed a reduction peak belonging to manganese oxide at 496 °C, and the reduction peak moved significantly to the low temperature region. However, with the reduction of cerium content, three reduction peaks attributed to cerium oxide in CM3 and CM4 catalysts could not be observed, because the amount of CeO_2 was too low, and part of Ce^{4+} was inserted into the lattice of Mn_2O_3. The reduction peak (334 °C) attributed to Mn_2O_3 reduction to Mn_3O_4 on CM4 catalyst is more forward, and the hydrogen consumption is also higher. Therefore, the catalyst still has strong redox activity. Combined with the results of XPS, the change of valence state of cerium–manganese ion also greatly affects the activity of the catalyst. Due to the presence of oxygen vacancies on the catalyst surface, gas phase O_2 and NO are adsorbed. According to the XPS results, the presence of Mn^{3+}, Mn^{4+}, Ce^{3+} and Ce^{4+} was detected in the catalyst. Therefore, the REDOX reaction of Mn^{3+}/Mn^{4+} or Ce^{3+}/Ce^{4+} contributes to the increase in the number of oxygen vacancies and NO adsorption (Fig. 4b).

To further explain the performance difference of NO oxidation, *in situ* Fourier infrared spectroscopy of adsorbed species on the catalyst were studied to obtain information about the types of NO_x species (Fig. 4). In Fig. 4c, four absorption peaks are observed on CeO_2, which are attributed to chelating bidentate nitrate (1573 cm^{-1}, 1290 cm^{-1} and 1027 cm^{-1}) and bridging nitrate (1448 cm^{-1}), respectively. As the reaction temperature gradually increases, bridging nitrate gradually decomposes. An absorption peak attributed to N_2O_4 (1360 cm^{-1}) appears.[52] Due to the strong adsorption of NO_x, a large number of chelated bidentate nitrates are produced. However, the bidentate nitrate cannot generate N_2O_4 with the increase of temperature, thus inhibiting the generation of N_2O_4.[53,54] In Fig. 4d, CM1 also has the obvious characteristic peaks of chelating bidentate nitrate (1573 cm^{-1}) and surface nitrate (1405 cm^{-1}),[55] and the surface nitrate gradually transforms into N_2O_4 with the increase in temperature. A new characteristic peak attributed to a bridging nitrate (1150 cm^{-1}) is generated from 350 °C.[56] This characteristic peak does not decompose with the increase of temperature so the catalytical activity is inhibited.[53] A weak characteristic peak of chelated bidentate nitrate (1573 cm^{-1}) can be seen in Fig. 4e, but this characteristic peak is not observed in Fig. 4f–h, suggesting that the adsorption of NO_x on CM2 is stronger than

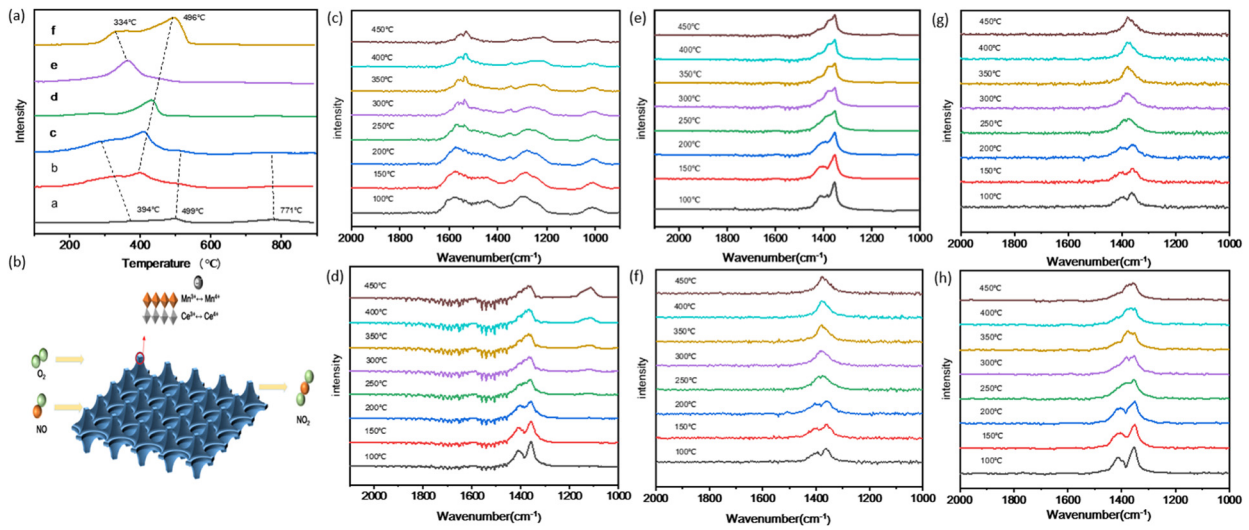

Fig. 4 (a) H_2-TPR profiles of cerium–manganese macroporous catalysts with different proportions. a. CeO_2, b. CM1, c. CM2, d. CM3, e. CM4, and f. Mn_2O_3. (b) Possible reaction mechanisms of 3DOM catalysts for NO_x oxidation. DRIFT spectra obtained on the catalysts: (c) CeO_2, (d) CM1, (e) CM2, (f) CM3, (g) CM4, and (h) Mn_2O_3.

that of CM3, CM4 and Mn_2O_3 catalysts. In addition, CM2 completely decomposed surface nitrate to form N_2O_4 at 250 °C, while CM3 and CM4 still have peaks belonging to surface nitrate at 250 °C. Therefore, the catalytical performance of CM2 catalyst is better than CM3 and CM4 at 250 °C. In short, compared with catalysts with a high cerium content, CM2 shows an adsorption strength promoting formation of a chelated bidentate nitrate, which is decomposed at high temperatures. Compared with the catalyst with a high manganese content, CM2 can adsorb NO to form a surface nitrate, which is decomposed at lower temperatures. Therefore, the CM2 proves to be an excellent catalyst for NO oxidation.

Conclusions

The ordered macroporous cerium–manganese composite oxides catalysts for NO oxidation were prepared by the sol–gel method. The ordered macroporous structure is about 300 nm and connected by pore windows of about 50 nm. These catalysts show a high specific surface area and thermal stability, and the large pore structure enables the pollutants to have better contact with the catalyst. Meanwhile, the synergistic effect of cerium–manganese increased the production of reactive oxygen species, and the formed cerium–manganese solid solution improved the catalytic oxidation performance, causing the NO oxidation reaction to move to the low temperature region. The catalyst with the best cerium–manganese ratio (1 : 2) can achieve a conversion rate of 62% at 250 °C, and the highest conversion rate was able to reach 98%, which is far higher than pure cerium oxide and pure manganese oxide catalysts. This work provides a promising catalyst for NO oxidation and soot combustion catalysts.

Conflicts of interest

There are no conflicts to declare.

Acknowledgements

We gratefully acknowledge the financial support from the National Key R&D Program of China (2022YFB3506200) and National Nature Science Foundation of China (Grant No. 22122113).

References

1 R. Agrawal, V. A. Wankhede, A. Kumar and S. Luthra, *Bus. Strategy Environ.*, 2021, **30**, 1051–1066.
2 Q. Zhao and M. Chen, *Resour., Conserv. Recycl.*, 2011, **57**, 15–21.
3 M. Contestabile, *Nat. Sustain.*, 2019, **2**, 10.
4 M. Brauer, B. Casadei, R. A. Harrington, R. Kovacs and K. Sliwa, *Circulation*, 2021, **143**, e800–e804.
5 J. Yang and B. Zhang, *Environ. Int.*, 2018, **120**, 443–455.
6 M. S. AlQahtani, S. D. Knecht, X. Wang, S. G. Bilén and C. Song, *ACS Catal.*, 2020, **10**, 5272–5277.
7 T. Bešenić, J. Baleta, K. Pachler and M. Vujanović, *Energy Convers. Manage.*, 2020, **217**, 112762.
8 S. Chen, Y. Li, M. Wang and X. Jiang, *Green Chem.*, 2020, **22**, 322–326.
9 S. Li, R. Liu, X. Jiang, Y. Qiu, X. Song, G. Huang, N. Fu, L. Lin, J. Song, X. Chen and H. Yang, *ACS Nano*, 2019, **13**, 2103–2113.
10 N. D. Wasalathanthri, T. M. SantaMaria, D. A. Kriz, S. L. Dissanayake, C.-H. Kuo, S. Biswas and S. L. Suib, *Appl. Catal., B*, 2017, **201**, 543–551.
11 Y. Zhang, D. Wang, Y. Pottimurthy, F. Kong, T.-L. Hsieh, B. Sakadjian, C. Chung, C. Park, D. Xu, J. Bao, L. Velazquez-Vargas, M. Guo, P. Sandvik, S. Nadgouda, T. J. Flynn, A. Tong and L.-S. Fan, *Appl. Energy*, 2021, **282**, 116065.
12 J. Gao, Y. Wang, S. Wang, X. Li, X. Chang, X. Wang, C. Yang and R. Xuan, *Chem. Eng. J.*, 2022, **443**, 136392.
13 A.-Y. Zhang, N.-H. Huang, C. Zhang, P.-C. Zhao, T. Lin, Y.-Y. He and J.-W. Feng, *Chem. Eng. J.*, 2018, **344**, 1–11.
14 Y. Jin, M. Li, F. Chen, L. Wang, L. Zhang, Z. Yang, N. Wang, J. Fu, Y. Yu, X. Cheng and D. Wu, *J. Hazard. Mater.*, 2023, **445**, 130523.
15 Y. Xia and X. Yang, *Acc. Chem. Res.*, 2017, **50**, 450–454.
16 C. S. McCallum, N. Strachan, S. C. Bennett, W. G. Forsythe, M. D. Garrett, C. Hardacre, K. Morgan and G. N. Sheldrake, *Green Chem.*, 2018, **20**, 2702–2705.
17 J. P. Hughes, J. Clipsham, H. Chavushoglu, S. J. Rowley-Neale and C. E. Banks, *Renewable Sustainable Energy Rev.*, 2021, **139**, 110709.
18 D. Banham, S. Ye, K. Pei, J. Ozaki, T. Kishimoto and Y. Imashiro, *J. Power Sources*, 2015, **285**, 334–348.
19 V. T. Nguyen, S. Riaño and K. Binnemans, *Green Chem.*, 2020, **22**, 8375–8388.
20 B. Wang, T. Chang, Z. Jiang, J. Wei and T. Fang, *Appl. Catal., B*, 2019, **251**, 261–272.
21 Z. Hou, L. Dai, Y. Liu, J. Deng, L. Jing, W. Pei, R. Gao, Y. Feng and H. Dai, *Appl. Catal., B*, 2021, **285**, 119844.
22 D. Malko, T. Lopes, E. Symianakis and A. R. Kucernak, *J. Mater. Chem. A*, 2015, **4**, 142–152.
23 S. T. Hunt, M. Milina, A. C. Alba-Rubio, C. H. Hendon, J. A. Dumesic and Y. Román-Leshkov, *Science*, 2016, **352**, 974–978.
24 Z. Li, J. Chu, D. Meng, Y. Wen, X. Xing, H. Miao, M. Hu, C. Yu, Z. Wei, Y. Yang and Y. Li, *ACS Catal.*, 2019, **9**, 8659–8668.
25 M. Li, X. Xing, Z. Ma, J. Lv, P. Fu and Z. Li, *ACS Sustainable Chem. Eng.*, 2018, **6**, 5495–5503.
26 J. Lv, B. Wang, J. Hao, H. Ding, L. Fan, R. Tao, H. Yang, J. Zhou and B. Lu, *eScience*, 2023, **3**, 100081.
27 L. Ni, R. Guo, S. Fang, J. Chen, J. Gao, Y. Mei, S. Zhang, W. Deng, G. Zou, H. Hou and X. Ji, *eScience*, 2022, **2**, 116–124.
28 Z. Li, J. Zhang, M. Li, X. Xing and Q. Zhang, *Nano Res.*, 2018, **11**, 80–88.
29 P. Zhang, M. Yang, D. Han, X. Liu, X. Yu, J. Xiong, Y. Li, Z. Zhao, J. Liu and Y. Wei, *Appl. Catal., B*, 2023, **321**, 122077.
30 Z. Meng, Z. Qiu, Y. Shi, S. Wang, G. Zhang, Y. Pi and H. Pang, *eScience*, 2023, **3**, 100092.
31 A. Setiabudi, J. Chen, G. Mul, M. Makkee and J. A. Moulijn, *Appl. Catal., B*, 2004, **51**, 9–19.

32 Y. Wei, Y. Zhang, P. Zhang, J. Xiong, X. Mei, Q. Yu, Z. Zhao and J. Liu, *Environ. Sci. Technol.*, 2020, **54**, 2002–2011.
33 J. H. Lee, S. H. Lee, J. W. Choung, C. H. Kim and K.-Y. Lee, *Appl. Catal., B*, 2019, **246**, 356–366.
34 V. Alcalde-Santiago, A. Davó-Quiñonero, D. Lozano-Castelló and A. Bueno-López, *Appl. Catal., B*, 2018, **234**, 187–197.
35 M. Zhao, J. Deng, J. Liu, Y. Li, J. Liu, Z. Duan, J. Xiong, Z. Zhao, Y. Wei, W. Song and Y. Sun, *ACS Catal.*, 2019, **9**, 7548–7567.
36 Z. Wang, Z. Tian, D. Han and F. Gu, *ACS Appl. Mater. Interfaces*, 2016, **8**, 5466–5474.
37 Y. Yakiyama, T. Hasegawa and H. Sakurai, *J. Am. Chem. Soc.*, 2019, **141**, 18099–18103.
38 J. Hu and L. Zhang, *J. Mater. Chem. A*, 2021, **9**, 27560–27567.
39 D. C. Grinter, M. Allan, H. J. Yang, A. Salcedo, G. E. Murgida, B.-J. Shaw, C. L. Pang, H. Idriss, M. V. Ganduglia-Pirovano and G. Thornton, *Angew. Chem.*, 2021, **60**, 13835–13839.
40 Y. Shao, B. Ren, H. Jiang, B. Zhou, L. Lv, J. Ren, L. Dong, J. Li and Z. Liu, *J. Hazard. Mater.*, 2017, **333**, 222–231.
41 P. Venkataswamy, K. N. Rao, D. Jampaiah and B. M. Reddy, *Appl. Catal., B*, 2015, **162**, 122–132.
42 J. Xiong, Y. Wei, Y. Zhang, P. Zhang, Q. Yu, X. Mei, X. Liu, Z. Zhao and J. Liu, *ACS Catal.*, 2020, **10**, 7123–7135.
43 X. Yu, Z. Zhao, Y. Wei, L. Zhao and J. Liu, *Catal. Sci. Technol.*, 2019, **9**, 1372–1386.
44 I. Gomaa, A. I. Abdel-Salam, A. Khalid and T. S. Soliman, *Opt. Laser Technol.*, 2023, **161**, 109126.
45 V. Alcalde-Santiago, A. Davó-Quiñonero, D. Lozano-Castelló and A. Bueno-López, *Appl. Catal., B*, 2018, **234**, 187–197.
46 T. Hu, Z. Fu, Z. Li, M. Liu, L. Zhang, Z. Yu, X. Chen, Y. Zheng, T. Li, Y. Wang, G. Wang, X. Dong and F. Xu, *ACS Appl. Mater. Interfaces*, 2021, **13**, 60241–60249.
47 J. Qian, J. Mo, Y. Zhou, M. Fan, Y. Chen, J. Liu, Y. Xu and S. Shen, *Mater. Chem. Phys.*, 2022, **285**, 126151.
48 X. Yu, Y. Ren, D. Yu, M. Chen, L. Wang, R. Wang, X. Fan, Z. Zhao, K. Cheng, Y. Chen, J. Gryboś, A. Kotarba, Z. Sojka, Y. Wei and J. Liu, *ACS Catal.*, 2021, **11**, 5554–5571.
49 M. Piumetti, B. van der Linden, M. Makkee, P. Miceli, D. Fino, N. Russo and S. Bensaid, *Appl. Catal., B*, 2016, **199**, 96–107.
50 D. Yu, L. Wang, C. Zhang, C. Peng, X. Yu, X. Fan, B. Liu, K. Li, Z. Li, Y. Wei, J. Liu and Z. Zhao, *ACS Catal.*, 2022, **12**, 15056–15075.
51 Y. Xin, L. Cheng, Y. Lv, J. Jia, D. Han, N. Zhang, J. Wang, Z. Zhang and X.-M. Cao, *ACS Catal.*, 2022, **12**, 397–410.
52 E. J. Lee, M. J. Kim, J. W. Choung, C. H. Kim and K.-Y. Lee, *Appl. Catal., A*, 2021, **627**, 118396.
53 Y. Liu, M. Meng, Z. Zou, X. Li and Y. Zha, *Catal. Commun.*, 2008, **10**, 173–177.
54 M. Ying, M. Zhang, Y. Liu and Z. Wu, *Sci. Rep.*, 2019, **9**, 14322.
55 U. Bentrup, A. Brückner, M. Richter and R. Fricke, *Appl. Catal., B*, 2001, **32**, 229–241.
56 L. Sivachandiran, F. Thevenet, A. Rousseau and D. Bianchi, *Appl. Catal., B*, 2016, **198**, 411–419.